The relation between the surface composition anomaly and the distribution of the exosphere of Mercury

Y. Suzuki[1], K. Yoshioka[1], G. Murakami[2], I. Yoshikawa[1]

[1] The University of Tokyo

[2] ISAS/JAXA

Corresponding author: Yudai Suzuki (yudai-suzuki127@g.ecc.u-tokyo.ac.jp)

Key Points:

- We discuss the correlation between Mercury's surface composition and exosphere distribution using observations by the MESSENGER spacecraft.
- Mg was found to have clear exosphere-surface correlation (ESC), Ca to have weak ESC, and Na to have little ESC.
- Conditions for components with ESC may include low volatility and small solar radiation acceleration.

Abstract

In celestial bodies with collisionless atmospheres, such as Mercury, the spatial distribution of the exosphere is expected to reflect the surface composition. In this study, we discuss whether the distribution of Mg, Ca, and Na, the primary exospheric components on Mercury, have exosphere-surface correlation (ESC) by analyzing the observation data of the Mercury Atmospheric and Surface Composition Spectrometer (MASCS) onboard the MErcury Surface, Space ENvironment, GEochemistry, and Ranging (MESSENGER) spacecraft. As a result, it was found that Mg has strong ESC, Ca has weak ESC and Na has little ESC. The Monte Carlo simulations of trajectory in the exosphere show that the weak ESC of Ca is due to the relatively large solar radiation acceleration. Na has ESC only in high-temperature regions around 0°E. This can be explained well by considering that the weakly physisorbed Na layer on the surface is depleted under high temperature and that the distribution of strongly chemisorbed Na atoms is reflected in the exosphere. Based on these results, the conditions for components with ESC in celestial bodies with thin atmospheres include low volatility and little solar radiation acceleration.

Plain Language Summary

In celestial bodies with very thin atmospheres, such as Mercury, most of the atmosphere originates directly from the surface. Therefore, it can be expected that the spatial distribution of the atmosphere maintains the surface composition. In this study, we examined whether the surface distributions of Mg, Ca and Na were reflected in the atmosphere using data collected by the MASCS onboard MESSENGER. As a result, the surface distributions of Mg, Ca, and Na were clarified to be strongly, weakly, and slightly reflected in the atmosphere, respectively. A simple numerical simulation shows that the Ca atmosphere does not correspond to the surface distribution well because Ca flows in the anti-sunward direction due to high solar radiation. It was also found that the surface Na distribution is linked to the atmosphere only in high-temperature regions. In celestial bodies with thin atmospheres, components with low volatility and small resonance scattering efficiency of solar radiation may correspond well to the surface distribution.

1 Introduction

Many celestial bodies in our solar system, such as Mercury, most moons, comets, and asteroids, have a thin and collisionless atmosphere, called the exosphere. Most of these atmospheres are directly supplied from the surface through several processes such as thermal desorption, photo-stimulated desorption (PSD), charged particle sputtering, and micro-meteoroid impact vaporization (MIV). The spatial structure of the thin atmosphere strongly depends on the surface composition and energy distribution when released. Because the surface distribution of some components corresponds to geological features, it is expected that the structure of the exosphere can be directly linked to the geology. In fact, the amount of Potassium (K) exosphere on the Moon is reported to increase over the KREEP regions (Colaprete et al., 2016; Rosborough et al., 2019). The surface composition distribution and geological features of some planets with thin atmospheres may be estimated by remote atmosphere observations.

On Mercury, Magnesium (Mg) in the exosphere is thought to have been ejected from the surface mainly through MIV because observations by the Mercury Atmospheric and Surface Composition Spectrometer (MASCS) onboard the MErcury Surface, Space ENvironment, GEochemistry, and Ranging (MESSENGER) spacecraft show that the Mg exosphere consists of high-energy atoms and has strong dawn-dusk asymmetry (Merkel et al., 2017). The surface Mg density distribution was obtained using an X-Ray Spectrometer (XRS) onboard MESSENGER, which revealed that Mg concentrates on the terrain around 280°E in the northern hemisphere (Weider et al., 2015). Merkel et al. (2018) indicated that the production rate of the Mg exosphere should be enhanced above this Mg-rich terrain by comparing MASCS data with XRS data. This is an interesting example of exosphere-surface correlation (ESC) on Mercury identified from observations.

Calcium (Ca) is also mainly ejected through MIV (Burger et al., 2014). In addition, Killen and Hahn (2015) and Christou et al. (2015) suggested that the impact of comet dust streams also contributes to the ejection of Ca exosphere in some seasons. The surface Ca distribution is known to be similar to that of Mg from the observations by XRS (Weider et al., 2015; Nittler et al., 2020). Ca is expected to have ESC since Ca is a refractory component and is mainly ejected by MIV along with Mg.

The Sodium (Na) exosphere is known to be divided into two components: a lower-energy component ejected through PSD and a higher-energy component ejected through MIV or sputtering (Cassidy et al., 2015). Surface Na in high temperature regions has been said to be depleted due to thermal desorption, though no atoms have been detected in the exosphere ejected through thermal desorption. The seasonal variability of Na exosphere is discussed in several model study such as Mura et al. (2009) and Leblanc and Johnson (2010). Cassidy et al. (2016) found that the amount of Na exosphere is enhanced at specific “cold-pole” longitude throughout the year. They attributed this phenomenon to the fact that the maximum temperature at these longitudes is lowest on Mercury due to the rotation-revolution

resonance. In contrast, Suzuki et al. (2020) suggested that additional Na ejection and supply of Na by dust streams' impact on these regions is also important for the enhancement, and Sarantos and Tsavachidis (2020) indicates that diffusion into the regolith also controls the amount of desorption. Although the cause of the seasonal variability of Na exosphere still remains as a big problem, there is no doubt that surface temperature greatly controls the amount of the exosphere throughout the Mercury year. Thus, the surface Na distribution is highly temperature-dependent and may not greatly reflect the geological features.

In summary, the current understanding predicts that Ca has clear ESC, as does Mg, and Na has almost no ESC on Mercury. In this study, we verified whether Mg, Ca, and Na on Mercury actually have ESC using observational data from the MASCS and XRS to understand the relation between the distribution of the exosphere and that of the surface composition of celestial bodies with thin atmospheres.

2 Analysis

First, we deduce the production rate of the exospheric component from the vertical profile obtained by MASCS. All the limb scan data from 2011 to 2015 were used for the analysis. The vertical profile of Mercury's exosphere is approximated by the Chamberlain's model (Chamberlain, 1963), as follows:

$$N(z) = 2KH(z)\zeta n_0 \, exp\left[\frac{-U(z)+U(0)}{k_B T}\right] \quad (1)$$

where z, n_0, T are the tangential altitude, near-surface density, and temperature, respectively. $2K$ is the ratio of the apparent column density to the vertical column density, which is approximated by:

$$2K \sim \sqrt{\frac{2\pi(R_{Me}+z)}{H(z)}} \quad (2)$$

$H(z)$ is defined by the following equation, similar to scale height:

$$H(z) = \frac{k_B T (R_{Me}+z)^2}{G M_{Me} M_{atom}} \quad (3)$$

where $M_{\mathrm{Me}}, M_{\mathrm{atom}}, R_{\mathrm{Me}}$ are the mass of Mercury, mass of atoms, and radius of Mercury, respectively. $U(z)$ is the potential of particles at altitude z expressed by the following equations:

$$U(z) = -\frac{G M_{Me} M_{atom}}{(R_{Me}+z)} + M_{atom} b \cos Z \, (R_{Me}+z) \quad (4)$$

where $b, \cos Z$ are the solar radiation acceleration, and cosine of the solar zenith angle, respectively. In equation (1), ζ is the partition function calculated by

$$\zeta = \frac{1}{2} + \frac{1}{2} erf\left(\sqrt{\lambda}\right) - \sqrt{\frac{\lambda}{\pi}} e^{-\lambda} - \frac{\sqrt{\lambda_0^2 - \lambda^2}}{2\lambda_0} e^{-\psi}\left(1 + erf\left(\sqrt{\lambda - \psi}\right)\right) + \sqrt{\frac{\lambda(\lambda_0 - \lambda)}{\pi\lambda_0}} e^{-\lambda} \quad (5)$$

where λ, λ_0 are the escape parameter at altitude z and at the surface defined as:

$$\lambda(z) = \frac{GM_{Me}M_{atom}}{k_B T(R_{Me} + z)}$$
$$\lambda_0 = \frac{GM_{Me}M_{atom}}{k_B T R_{Me}} \quad (6)$$

and ψ is defined as:

$$\psi(z) = \frac{\lambda(z)^2}{\lambda(z) + \lambda_0} \quad (7)$$

The Chamberlain's model does not take into account the photoionization. However, photoionization is not effective in the observation range of MESSENGER since typical flight scales (the product of photoionization lifetime and the thermal velocity) of Mg, Ca and Na at a heliocentric distance of 0.4 au are, respectively, about $10^{6.5}$ km, $10^{4.5}$ km and 10^5 km.

The apparent column density $N(z)$ in cm^{-2} is derived from the observed radiance $4\pi I$ in Rayleigh from the following conversion formula:

$$N\ (cm^{-2}) = 10^6 \frac{4\pi I}{g} \quad (8)$$

where g is the solar photon scattering probability (known as g-factor). The g-factor is assumed to be uniform in a single TAA, although it originally has a standard deviation of about 30% due to the variation depending on the radial velocity against the Sun. The production rate S is estimated by the product of the near-surface density and first-order moment of velocity.

$$S = n_0 \int_0^\infty v^2 dv \int_{\theta=\frac{\pi}{2}}^{\theta=0} d\cos\theta \int_0^{2\pi} d\phi\, f(v,T)\, v$$
$$= \frac{n_0}{2} \sqrt{\frac{2k_B T}{\pi M_{atom}}} \quad (9)$$

$f(v,T)$ in the equation is the Maxwellian distribution.

We used the Levenberg-Marquardt method to estimate the near-surface density n_0 and temperature T from the vertical profile through fitting with the model profile (Fig. 1). For Mg and Ca, because some data showed an unknown sharp

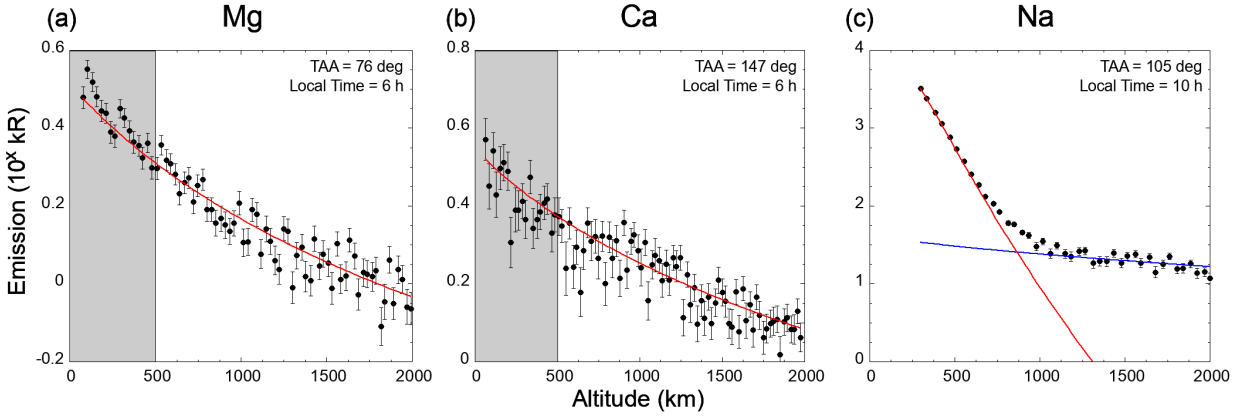

Fig. 1: Fitting to the vertical profile of (a) Mg, (b) Ca, and (c) Na.

For Mg and Ca, fitting was performed while ignoring the observations with tangential altitude is lower than 500 km (the gray region). The Na vertical profile was fitted assuming two components: a lower-energy component and a higher-energy component, and only the production rate of the lower-energy component derived from PSD was used. The Levenberg-Marquardt method was used for fitting.

increase in brightness at low altitudes (gray-hatched in the figure), possibly due to uncorrected scattering from the bright surface, we used only data above 500 km for fitting (Fig. 1(a)). For Na, because it is difficult to precisely evaluate the production rate of higher-energy components due to the low signal to noise ratio of the data or to the limitgs of the adopted physical model as pointed out in Cassidy et al. (2015), we used only the production rate of the lower-energy component, which was ejected through PSD (Fig. 1(b)). The production rate of Mg and Ca is comparable to the one estimated in Merkel et al. (2017) and Burger et al. (2014), respectively.

To remove the effect of seasonal variability, the production rate is devided by that at the antipodal points at the same TAA, the same local time and the different Mercury year. Then, We defined a "relative production parameter" Σ at the tangential point longitude of ϕ, TAA of α, and local time of h, as follows:

$$\Sigma(\phi,\alpha,h) \equiv log_{10}\left(\frac{S(\phi,\alpha,h)}{S(\phi+\pi,\alpha,h)}\right) \quad (10)$$

When calculating Σ, we averaged the production rate S obtained from the data for each local time 2 h and TAA 4°. Since the seasonal variation is offset through this calcuration, $\Sigma(\phi,\alpha,h)$ is expected to strongly depend on the ratio of surface abundance. Note that $\Sigma(\phi,\alpha,h) > 0$ means $S(\phi,\alpha,h) > S(\phi+\pi,\alpha,h)$, and $\Sigma(\phi,\alpha,h) = -\Sigma(\phi+\pi,\alpha,h)$. For Mg and Ca, the correlation coefficient between $\Sigma(\phi)$ and the surface Mg and Ca abundance ratio, $\log_{10}\left(\sigma(\phi)/\sigma(\phi+\pi)\right)$, where σ is the surface density of Mg and Ca around the equator, is calculated. The surface density

distribution of Mg and Ca (Fig. 2) is derived from Nittler et al. (2020). Surface Na density in the northern hemisphere was presumed by Peplowski et al. (2014) based on observations by the Gamma-Ray Spectrometer (GRS) onboard MESSENGER. However, the production rate of Na exosphere cannot be compared to the surface Na density since the exosphere data concentrated around the equator do not spread in the latitude direction and the surface data, on the other hand, have little information in the longitude direction.

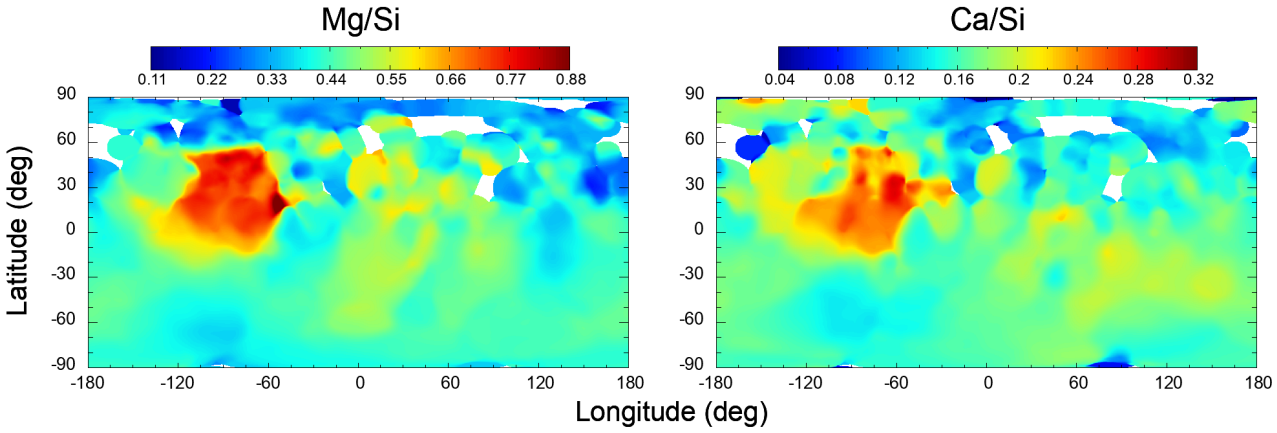

Fig. 2: The surface density distribution of (a) Mg and (b) Ca deduced from the observations by MESSENGER/XRS.

3 Results and Discussion

3.1 Mg

The relative production parameters of Mg (the colored dots) and surface Mg abundance ratio at the equator (the black solid line) as a function of longitude are plotted in Fig. 3(a). Data points are concentrated around the $\pm 90°$ due to the geometry of MESSENGER. In all the analyses below, including those of Ca and Na, we have systematically removed noisy data (with relative error of $S(\phi)/S(\phi + \pi)$ greater than 10%). The correlation coefficient between the production rate ratio and surface abundance ratio was $r = 0.70 \pm 0.17$, with a 95% confidence interval of $0.65 < r < 0.76$. The number of data used in this study was increased compared to that of the previous study (Merkel et al., 2018), which used only local time 06 data. In addition, calculating the surface Mg abundance ratio in the same way as the production rate of the Mg exosphere enabled statistical tests using the correlation coefficient, which clarifies the ESC for Mg on Mercury.

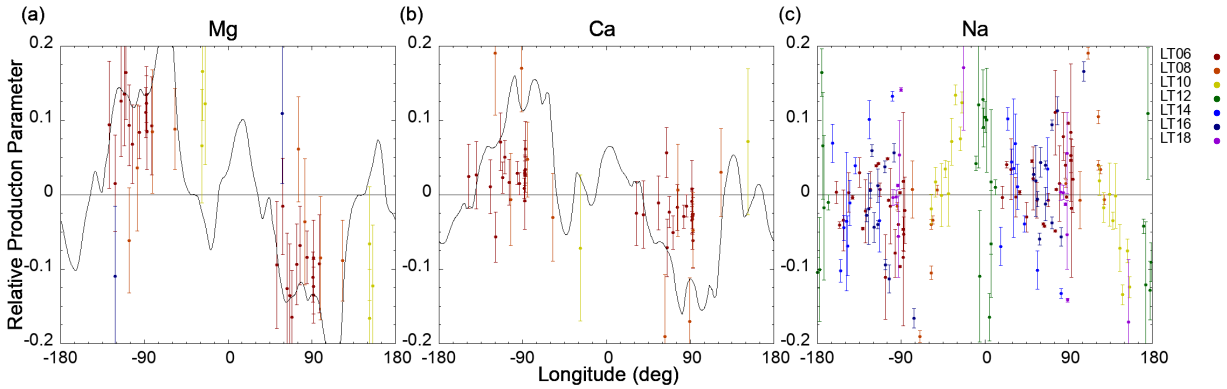

Fig. 3: The dependence of the relative production parameter on longitude.

The dot color represents the local time at which the observations was performed. The black solid line in (a) and (b) is the surface Mg abundance ratio.

191

192 3.2 Ca

193 The relative production parameters of Ca (the colored dots) and surface Ca
194 abundance ratio at the equator (the black solid line) as a function of longitude are
195 plotted in Fig. 3(b). The correlation coefficient between the production rate ratio and
196 surface abundance ratio was $r = 0.22 \pm 0.14$, with a 95% confidence interval of $0.12 <$
197 $r < 0.32$. This result indicates that the ESC of Ca is much weaker than that of Mg.
198 We consider that the difference between these results is due to the fact that
199 the g-factor of Ca is approximately ten times larger than that of Mg. As a result, Ca
200 experiences more solar radiation acceleration and is more likely to flow in the
201 tailward direction. To confirm this difference between the two components, we
202 performed three-dimensional Monte Carlo simulations of the trajectories of Ca and
203 Mg atoms in the exosphere. In this model, 10,000 atoms of Mg or Ca are ejected only
204 once from the point of 280°E (the red arrow), which Mg and Ca concentrate on, and
205 they move affected by gravity of Mercury and the Sun and solar radiation pressure.
206 The g-factor is set to be a function of radial velocity with respect to the Sun. We
207 assume that Mercury is at perihelion, or TAA = 0°. Fig. 4 shows the distribution of
208 Ca and Mg atoms in 60 min after ejection, seen from the south as well as the
209 observations by the MASCS. Killen et al. (2005) suggested that Ca is first released
210 as a form of CaO and dissociates into high-energy Ca atoms under UV irradiation,
211 while Valiev et al. (2017) showed that energetic Ca in the exosphere is not
212 generated from CaO. So, the source of Ca has not been identified yet. Although our
213 calculation used several energies in the range of 3,000K to 40,000K, the qualitative
214 results were the same as those in Fig. 4, which is the case of 20,000K. These results
215 show that information on distribution of the surface Ca is moved in the tailward by
216 solar radiation. This makes the ESC computationally smaller since our method

using Chamberlain model ignores the horizontal transport when estimating production rate.

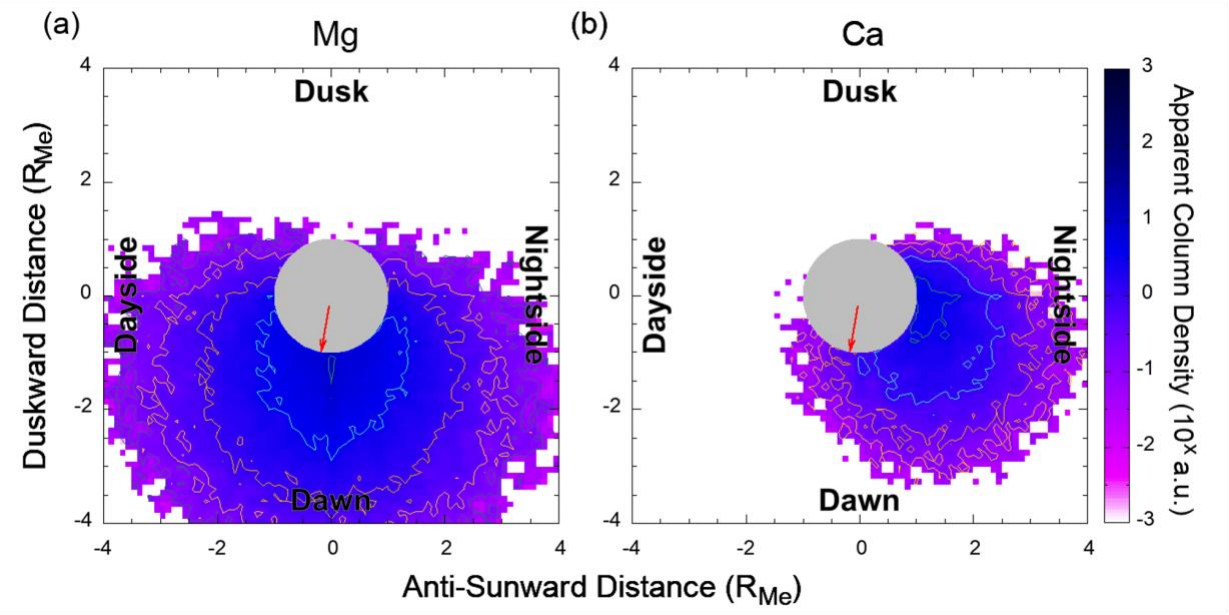

Fig. 4: Trajectories of Mg and Ca atoms using test particle simulations at perihelion. The color scale, which is displayed on a logarithmic scale, corresponds to the line-of-sight integration of the amount of the exosphere seen from the south as well as the observations by the MASCS. Note that the absolute value of the color scale does not have physical meaning. It can be seen that Ca tends to flow in the anti-sunward direction, unlike Mg.

3.3 Na

The relative production parameter of Na (the colored dots) as a function of longitude is plotted in Fig. 3(c). Because Na has a larger amount of data due to its brightness, we will discuss using only the data with relative error of $S(\phi)/S(\phi+\pi)$ is less than 5% instead of 10% (Fig. 5(a)). The relative production parameter Σ is close to 0 at most longitudes, but we can see $\Sigma > 0$ in the region of $-45°$E to 0°E (red box in Fig. 5(a)). This region has especially high maximum temperature, reaching 650K at perihelion. When we extract only the region whose temperature when the

data were collected is high (>550K), we can find that $\Sigma > 0$ in the region of −45°E to 45°E (red box in Fig. 5(b)), which means that production rate of Na exosphere in

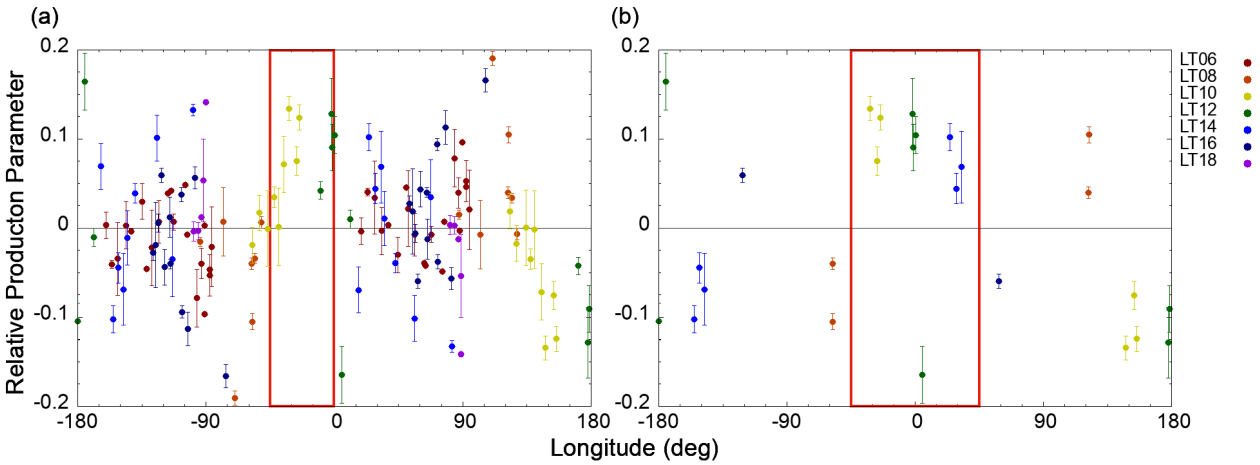

Fig. 5: The dependence of the Na relative production parameter on longitudes. (a) Data with relative error of $S(\phi)/S(\phi+\pi)$ is less than 5% are plotted. (b) Data with relative error of $S(\phi)/S(\phi+\pi)$ is less than 5% and with temperature above 550K are plotted. The colors of each dot represents the local time when the observation was performed.

45°E to −45°E is larger than in 135°E to −135°E (Fig. 5(b)).

The cause of $\Sigma > 0$ in the region of −45°E to 45°E can be explained well by assuming two methods of Na surface binding: physisorption and chemisorption. Similar ideas have often been assumed in the Na exosphere models, such as the one by Leblanc and Johnson (2010). Most of the physisorbed components consists of Na atoms that re-impact the surface. Since they are easily ejected through thermal desorption owing to their binding energy being less than 2.0 eV, the distribution

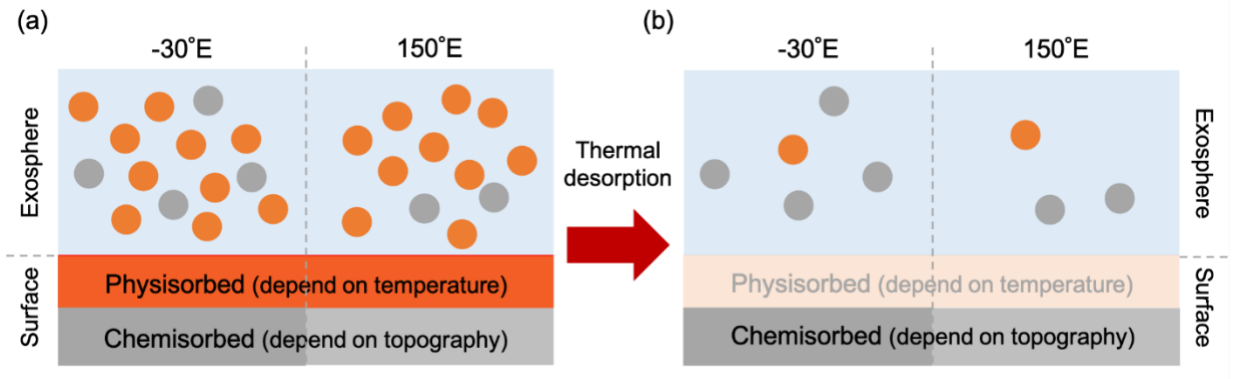

Fig. 6: A two-layer scenario of the surface Na.
(a) At the intermediate temperature of about 500 K, the exosphere mainly consists of physisorbed Na atoms. (b) When the surface temperature rises, the physisorbed Na layer is depleted, and chemisorbed Na atoms occupy the exosphere. Thus, ESC is considered to appear in the extremely high-temperature regions.

mainly corresponds to surface temperature. In contrast, the binding energy of chemisorbed Na atoms is approximately 2.6 eV assuming, for example, Na-O bond

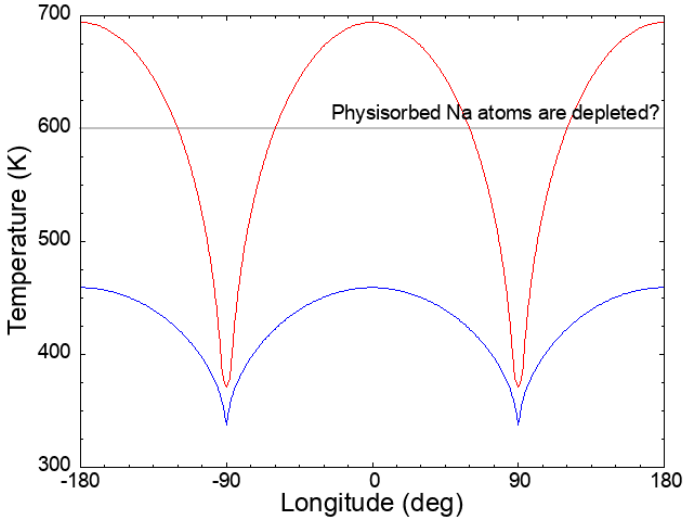

Fig. 7: The surface temperature experienced by each longitude.
The red line shows the maximum temperature and the blue line shows the average temperature which each region experiences during Mercury's revolution.

(Bida et al., 2000), which implies chemisorbed Na are distributed depending not only on surface temperature but on geological features.

The possible scenario is as follows (Fig. 6): when the surface temperature is intermediate (lower than approximately 500K), the thermal accommodation layer, which is composed of physisorbed atoms, is not depleted, and most of the produced Na exosphere is derived from the physisorbed component. Therefore, the production rate of the exosphere mainly depends on the surface temperature and UV flux. However, in the high-temperature region above 550 K, such as around 0°E (Fig.7), the physisorbed Na atoms are depleted by thermal desorption or diffusion into the subsurface, and most of the ejected Na is occupied by the chemisorbed atoms. Thus, the production rate of the exosphere also begins to depend on geological features, that is, ESC appears in the high-temperature regions from −45°E to 45°E (and from 135°E to −135°E). Parameters related to thermal desorption, such as binding energy and oscillation frequency, have not been determined well: Hunten and Sprague (2002) adopted 1.4 eV and 10^{13} Hz, Leblanc and Johnson (2010) used a Gaussian distribution between 1.4 and 2.7 eV with a most probable value of 1.85 eV and 10^{9}-10^{11} Hz, Suzuki et al., (2020) assumed 1.85 eV and 10^{13} Hz (Fig. 8), and Sarantos and Tsavachidis (2020) demonstrated that diffusion makes the energy barrier of the desorption higher. It typically takes about 10 min for thermally desorbed atoms to re-impact the surface. If a binding energy is less than 1.85 eV and oscillation frequency is larger than 10^{13} Hz, the desorption rate per 10 minutes reaches nearly 100 % in regions with temperature above 550 K, which is consistent with our results. Note that the regions with larger production rate do not always correspond

263 to surface composition anomaly, since solar radiation acceleration of Na is even
264 larger than that of Ca. Besides, the composition anomaly of chemisorbed component
265 does not always reflect on the geological history of Mercury, since it also gradually
266 varies through repeated thermal desorption.

267

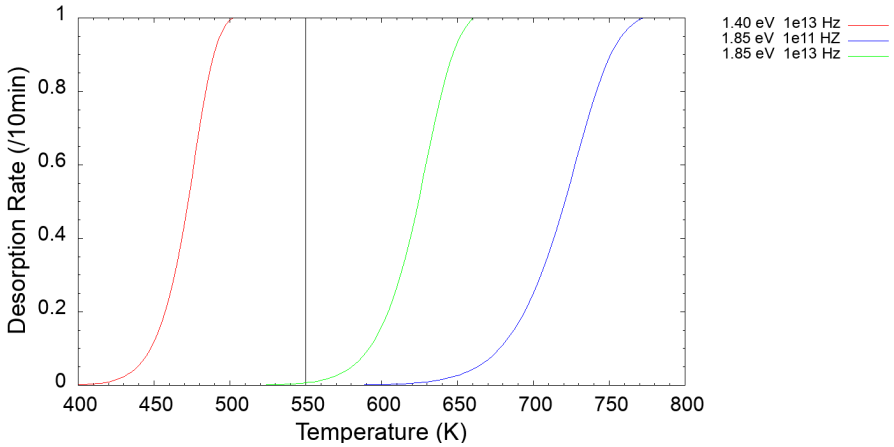

Fig. 8: Parameter dependence of the thermal desorption rate.
The red and green lines use parameter sets adopted by Hunten and Sprague (2002) and Suzuki et al., (2020), respectively. The blue line uses parameters assumed as the most probable values by Leblanc and Johnson (2010). Each line represents the proportion of thermally desorbed Na from the surface.

268 3.4 Implication for other components

269 From the discussion above, low volatility and small solar radiation
270 acceleration are important factors for ESC. Additionally, long photoionization
271 lifetime may also be important, although this was not found in our study.
272 Photoionized atoms orbit under the influence of an electromagnetic field. Since
273 neutral atoms with a short photoionization lifetimes in the exosphere include most
274 atoms that have undergone photoionization and re-neutralization, their distribution
275 is greatly affected by the electromagnetic field and will no longer reflect the
276 geological features. Therefore, a shorter photoionization lifetime is expected to
277 weaken ESC, except at very low altitudes. This would be verified when the
278 distribution of atoms with extreme short photo-ionization lifetime such as
279 Aluminium is observed.
280 The solar radiation acceleration and photoionization lifetimes of some of the
281 components of Mercury's exosphere are shown in Table 1. The solar radiation
282 acceleration of atoms was calculated using the following equation.

283 $$b = \frac{1}{m_{atom}} \sum_i \frac{h}{\lambda_i} g_i \qquad (11)$$

where $m_{\mathrm{atom}}, h, \lambda_i, g_i$ are the mass of atoms, plank constant, wavelength of each emission line, and g-factor, respectively. The g-factor was calculated using values from Killen et al. (2009). As g-factor, that at rest and at 1 au is used. The photoionization lifetime was derived from Fulle et al. (2007).

Considering the constants in Table 1, Oxygen and Sulfer have small solar radiation acceleration and long photoionization lifetimes, which suggest existence of ESC on Mercury. Although Na and K are more thermally desorbed, it has been reported that the amount of Na in the Moon's exosphere increases above low-albedo regions (Colaprete et al., 2016) and that of K is enhanced above the KREEP region (Rosborough et al., 2019). In celestial bodies far from the central star, even atoms that are thermally desorbed more easily, with larger solar radiation acceleration or with shorter photoionization lifetimes, may have ESC.

Component	Solar radiation acceleration at 1 au (m/s^2)	Photoionization lifetime @1 au (s)	ESC on Mercury
Na	2.5×10^{-2}	1.9×10^{5}	Little
K	2.1×10^{-4}	4.3×10^{4}	Little?
Mg	1.9×10^{-3}	2.1×10^{6}	Strong
Ca	1.3×10^{-2}	1.4×10^{4}	Weak
O	2.5×10^{-6}	2.0×10^{6}	Strong?
S	4.4×10^{-6}	4.2×10^{5}	Strong?

Table 1: The solar radiation acceleration and photoionization lifetime of each atom at 1 au.
Solar radiation acceleration is estimated using the g-factor calculated in Killen et al. (2009), and the photoionization lifetime is derived from Fulle et al. (2007). Although Na and K seem to have ESC in terms of solar radiation acceleration and photoionization, they are expected not to have ESC due to the fluctuations in surface density through thermal desorption and re-impact.

5 Conclusion

In celestial bodies with thin atmospheres, atoms are supplied from the surface to the exosphere due to the effects of the space environment, such as heating, UV radiation, and the impact of micro-meteoroids. Thus, the spatial distribution of some components in the exosphere is expected to reflect the distribution of each component on the surface as well as geological features such as craters and volcanic terrain. In this study, we verified the existence of ESC on Mercury using observations by MASCS and XRS onboard MESSENGER. As a result, we clearly showed that Mg has strong ESC, as suggested by Merkel et al.

(2018), and that Ca has weak ESC. Based on simple Monte Carlo simulations, we attributed this weak ESC of Ca to the effective tailward transportation by solar radiation acceleration. Although Na atoms are easily desorbed thermally, it is possible that ESC appears in the high-temperature region due to the depletion of the physisorbed Na layer on the surface. Based on these results, we considered that volatility and solar radiation acceleration control the ESC. S and O may also have ESC on Mercury, and it is expected that ESC will be found in various components on cooler celestial bodies such as Europa and Ganymede.

The presence or absence of ESC is a very interesting and useful issue, but there have not been enough observational data to discuss this. We hope that observations by the BepiColombo mission (Milillo et al., 2020; Murakami et al., 2020), launched in 2018, will allow us to discuss this issue in more detail. This will provide us with insights in the latitude direction — we could only discuss the distribution in the longitude direction in this study. The MSASI (Yoshikawa et al., 2010) onboard the Mio spacecraft will provide the detailed structure of the Na exosphere. PHEBUS (Quémerais et al., 2020) and SERENA (Orsini et al., 2021) onboard the MPO spacecraft will clarify the distribution of a variety of components in the exosphere, and MERTIS (Hiesinger et al., 2020) onboard MPO will reveal a wide range of surface material distributions on Mercury.

Acknowledgments, Samples, and Data

The original data reported in this paper are archived by Izenberg, N. (2018). Izenberg PDART 2014 MESSENGER Advanced Products Bundle. Geosciences Node. (https://doi.org/10.17189/1518648). The calculation results are archived at https://doi.org/10.5281/zenodo.5375947 (Suzuki et al., 2021).

References

Bida, T. A., Killen, R. M., & Morgan, T. H. (2000). Discovery of calcium in Mercury's atmosphere. *Nature*, 404, 159-161. doi:10.1038/35004521

Burger, M. H., Killen, R. M., McClintock, W. E., Merkel, A. W., Vervack, R. J. Jr., Cassidy, T. A., & Sarantos, M. (2014). Seasonal variations in Mercury's dayside calcium exosphere. *Icarus*, 238, 51–58. doi:10.1016/j.icarus.2014.04.049

Cassidy, T. A., McClintock, W. E., Killen, R. M., Sarantos, M., Merkel, A. W., Vervack, R. J. Jr., & Burger, M. H. (2016). A cold-pole enhancement in

Mercury's sodium exosphere. *Geophysical Research Letters*, 43, 11,121–11,128. doi:10.1002/2016GL071071

Cassidy, T. A., Merkel, A. W., Burger, M. H., Sarantos, M., Killen, R. M., McClintock, W. E., & Vervack, R. J. Jr. (2015). Mercury's seasonal sodium exosphere: MESSENGER orbital observations. *Icarus*, 248, 547–559. doi:10.1016/j.icarus.2014.10.037

Chamberlain, J. W. (1963). Planetary coronae and atmospheric evaporation. *Planetary and Space Science*, 11, 911–960. doi:10.1016/0032-0633(63)90122-3

Christou, A. A., Killen, R. M., & Burger, M. H. (2015). The meteoroid stream of comet Encke at Mercury: Implications for MErcury Surface, Space ENvironment, GEochemistry, and Ranging observations of the exosphere. *Geophysical Research Letters*, 42, 7311–7318. doi:10.1002/2015GL065361

Colaprete, A., Sarantos, M., Wooden, D. H., Stubbs, T. J., Cook, A. M., Shirley, M. (2016). How surface composition and meteoroid impacts mediate sodium and potassium in the lunar exosphere. *Science*, 351, 249-252. doi:10.1126/science.aad2380

Fulle, M., Leblanc, F., Harrison, R. A., Davis, C. J., Eyles, C. J., Halain, J. P., Howard, R. A., Bockelée-Morvan, D., Cremonese, G., Scarmato, T. (2007). Discovery of the atomic iron tail of comet McNaught using the heliospheric imager on STEREO. *The Astrophysical Journal*, 661(1), L93–L96. doi:10.1086/518719

Hiesinger, H., Helbert, J., Alemanno, G., Bauch, K. E., D'Amore, M., Maturilli, A., Morlok, A., Reitze, M. P., Stangarone, C., Sojic, A. N., Varatharajan, I., Weber, I., the MERTIS Co-I Team. (2020). Studying the Composition and Mineralogy of the Hermean Surface with the Mercury Radiometer and Thermal Infrared Spectrometer (MERTIS) for the BepiColombo Mission: An Update. *Space Science Review*, 216:110. doi:10.1007/s11214-020-00732-4

Hunten, D. M., & Sprague, A. L. (2002). Diurnal variation of sodium and potassium at Mercury. *Meteoritics and Planetary Science*, 37, 1191–1195. doi:10.1111/j.1945-5100.2002.tb00888.x

Izenberg, N. (2018). Izenberg PDART 2014 MESSENGER Advanced Products Bundle. Geosciences Node. doi:10.17189/1518648

Killen, R. M., Bida, T. A., & Morgan, T. H. (2005). The calcium exosphere of Mercury. *Icarus*, 173, 300-311. doi:10.1016/j.icarus.2004.08.022

Killen, R. M., & Hahn, J. M. (2015). Impact vaporization as a possible source of Mercury's calcium exosphere. *Icarus*, 250, 230–237. doi:10.1016/j.icarus.2014.11.035

Killen, R. M., Shemansky, D., & Mouawad, N. (2009). Expected emission from Mercury's exospheric species, and their ultraviolet-visibile signitures. *Astrophysics Journal Supplement*, 181, 351–359. doi:10.1088/0067-0049/181/2/351

Leblanc, F., & Johnson, R. E. (2010). Mercury exosphere I. Global circulation model of its sodium component. *Icarus*, 209, 280–300. doi:10.1016/j.icarus.2010.04.020

Merkel, A. W., Cassidy, T. A., Vervack, R. J. Jr., McClintock, W. E., Sarantos, M., Burger, M. H., & Killen, R. M. (2017). Seasonal variations of Mercury's magnesium dayside exosphere from MESSENGER observations. *Icarus*, 281, 46–54. doi:10.1016/j.icarus.2016.08.032

Merkel, A.W., Vervack Jr., R. J., Killen, R. M., Cassidy, T. A., McClintock, W. E., Nittler, L. R., & Burger, M. H. (2018). Evidence Connecting Mercury's Magnesium Exosphere to Its Magnesium-Rich Surface Terrane. *Geophysical Research Letters*, 45, 6,790-6,797. doi:10.1029/2018GL078407

Milillo, A., Fujimoto, M., Murakami, G., Benkhoff, J., Zender, J., Aizawa, S., Dósa, M., Griton, L., Heyner, D., Ho, G., Imber, S. M., Jia, X., Karlsson, T., Killen, R. M., Laurenza, M., Lindsay, S. T., McKenna-Lawlor, S., Mura, A., Raines, J. M., Rothery, D. A., André, N., Baumjohann, W., Berezhnoy, A., Bourdin, P. A., Bunce, E. J., Califano, F., Deca, J., de la Fuente, S. Dong, C., Grava, C., Fatemi, S., Henri, P., Ivanovski, S. L., Jackson, B. V., James, M., Kallio, E., Kasaba, Y., Kilpua, E., Kobayashi, M., Langlais, B., Leblanc, F., Lhotka, C., Mangano, V., Martindale, A., Massetti, S., Masters, A., Morooka, M., Narita, Y., Oliveira, J. S., Odstrcil, D., Orsini, S., Pelizzo, M. G., Plainaki, C., Plaschke, F., Sahraoui, F., Seki, K., Slavin, J. A., Vainio, R., Wurz, P., Barabash, S., Carr, C. M., Delcourt, D., Glassmeier, K. -H., Grande, M., Hirahara, M., Huovelin, J., Korablev, O., Kojima, H., Lichtenegger, H., Livi, S., Matsuoka, A., Moissl, R., Moncuquet, M., Muinonen, K., Quèmerais, E., Saito, Y., Yagitani, S., Yoshikawa, I., Wahlund, J. -E. (2020). Investigating Mercury's Environment with the Two-Spacecraft BepiColombo Mission. *Space Science Review*, 216:93. doi:10.1007/s11214-020-00712-8

Mura, A., Wurz, P., Lichtenegger, H. I. M., Schleicher, H., Lammer, H., Delcourt, D., Milillo, A., Orsini, S., Massetti, S., & Lhodachenko, M. L. (2009). The sodium exosphere of Mercury: Comparison between observations during

Mercury's transit and model results. Icarus, 200, 1-11. doi:10.1016/j.icarus.2008.11.014

Murakami, G., Hayakawa, H., Ogawa, H., Matsuda, S., Seki, T., Kasaba, Y., Saito, Y., Yoshikawa, I., Kobayashi, M., Baumjohann, W., Matsuoka, A., Kojima, H., Yagitani, S., Moncuquet, M., Wahlund, J. -E., Delcourt, D., Hirahara, M., Barabash, S., Korablev, O., Fujimoto, M. (2020). Mio—First Comprehensive Exploration of Mercury's Space Environment: Mission Overview. *Space Science Review*, 216:113. doi:10.1007/s11214-020-00733-3

Nittler, L. R., Frank, E. A., Weider, S. Z., Crapster-Pregont, E., Vorburger, A., Starr, R. D., Solomon, S. C. (2020) Global major-element maps of Mercury from four years of MESSENGER X-Ray Spectrometer observations. *Icarus*, 345, 113716. doi: 10.1016/j.icarus.2020.113716

Orsini, S., Livi, S. A., Lichtenegger, H., Barabash, S., Milillo, A., De Angelis, E., Phillips, M., Laky, G., Wieser, M., Olivieri, A., Plainaki, C., Ho, G., Killen, R. M., Slavin, J.A., Wurz, P., Berthelier, J.-J., Dandouras, I., Kallio, E., McKenna-Lawlor, S., Szalai, S., Torkar, K., Vaisberg, O., Allegrini, F., Daglis, I. A., Dong, C., Escoubet, C. P., Fatemi, S., Fränz, M., Ivanovski, S., Krupp, N., Lammer, H., Leblanc, François., Mangano, V., Mura, A., Nilsson, H., Raines, J.M., Rispoli, R., Sarantos, M., Smith, H. T., Szego, K., Aronica, A., Camozzi, F., Di Lellis, A. M., Fremuth, G., Giner, F., Gurnee, R., Hayes, J., Jeszenszky, H., Tominetti, F., Trantham, B., Balaz, J., Baumjohann, W., Brienza, D., Bührke, U., Bush, M. D., Cantatore, M., Cibella, S., Colasanti, L., Cremonese, G., Cremonesi, L., D'Alessandro, M., Delcourt, D., Delva, M., Desai, M., Fama, M., Ferris, M., Fischer, H., Gaggero, A., Gamborino, D., Garnier, P., Gibson, W. C., Goldstein, R., Grande, M., Grishin, V., Haggerty, D., Holmström, M., Horvath, I., Hsieh, K. -C., Jacques, A., Johnson, R. E., Kazakov, A., Kecskemety, K., Krüger, H., Kürbisch, C., Lazzarotto, F., Leblanc, Frederic., Leichtfried, M., Leoni, R., Loose, A., Maschietti, D., Massetti, S., Mattioli, F., Miller, G., Moissenko, D., Morbidini, A., Noschese, R., Nuccilli, F., Nunez, C., Paschalidis, N., Persyn, S., Piazza, D., Oja, M., Ryno, J., Schmidt, W., Scheer, J. A., Shestakov, A., Shuvalov, S., Seki, K., Selci, S., Smith, K., Sordini, R., Svensson, J., Szalai, L., Toublanc, D., Urdiales, C., Varsani, A., Vertolli, N., Wallner, R., Wahlstroem, P., Wilson, P., Zampieri, S. (2021). SERENA: Particle Instrument Suite for Determining the Sun-Mercury Interaction from BepiColombo. *Space Science Review*, 217:11. doi:10.1007/s11214-020-00787-3

Peplowski, P. N., Evans, L. G., Stockstill-Cahill, K. R., Lawrence, D. J., Goldsten, J. O., McCoy, T. J., Nittler, L. R., Solomon, S. C., Sprague, A. L., Starr, R. D., & Weider, S. Z. (2014). Enhanced sodium abundance in Mercury's north polar region revealed by the MESSENGER Gamma-Ray Spectrometer. *Icarus*, 228, 86-95. doi:10.1016/j.icarus.2013.09.007

Quémerais, E., Chaufray, J. -Y., Koutroumpa, D., Leblanc, F., Reberac, A., Lustrement, B., Montaron, C., Mariscal, J. -F. Rouanet, N., Yoshikawa, I., Murakami, G., Yoshioka, K., Korablev, O., Belyaev, D., Pelizzo, M. G., Corso, A., Zuppella, P. (2020). PHEBUS on Bepi-Colombo: Post-launch Update and Instrument Performance. *Space Science Review*, 216:67. doi:10.1007/s11214-020-00695-6

Rosborough, S. A., Oliversen, R. J., Mierkiewicz, E. J., Sarantos, M., Robertson, S. D., Kuruppuaratchi, D. C. P., Derr, N. J., Gallant, M. A., & Roesler, F. L. (2019). High-Resolution Potassium Observations of the Lunar Exosphere. *Geophysical Research Letters*, 46, 6,964-6,971. doi:10.1029/2019GL083022

Sarantos, M., & Tsavachidis, S. (2020). The Boundary of Alkali Surface Boundary Exospheres of Mercury and the Moon. *Geophysical Research Letters*, 47(16), e2020GL088930. doi:10.1029/2020GL088930

Suzuki, Y., Yoshioka, K., Murakami, G., & Yoshikawa, I. (2020). Seasonal variability of Mercury's sodium exosphere deduced from MESSENGER data and numerical simulation. *Journal of Geophysical Research: Planets*, 125, e2020JE006472. doi:10.1029/2020JE006472

Suzuki, Y., Yoshioka, K., Murakami, G., & Yoshikawa, I. (2021). The relation between the surface composition anomaly and the distribution of the exosphere of Mercury [data set]. Zenodo. doi:10.5281/zenodo.5375947

Valiev, R. R., Berezhnoy, A. A., Sodorenko, A. D., Merzlikin, B. S., & Cherepanov, V. N. (2017). Photolysis of metal oxides as a source of atoms in planetary exospheres. *Planetary and Space Science*, 145, 38-48. doi:10.1016/j.pss.2017.07.011

Weider, S. Z., Nittler, L. R., Starr, R. D., Crapster-Pregont, E. J., Peplowski, P. N., Denevi, B. W., Head, J. W., Byrne, P. K., Hauck II, S. A., Ebel, D. S., & Solomon, S. C. (2015). Evidence for geochemical terranes on Mercury: Global mapping of major elements with MESSENGER's X-Ray Spectrometer. *Earth and Planetary Science Letters*, 416, 109-120. doi:10.1016/j.epsl.2015.01.023

Yoshikawa, I., Korablev, O., Kameda, S., Rees, D., Nozawa, H., Okano, S., Gnedykh, V., Kottsov, V., Yoshioka, K., Murakami, G., Ezawa, F., & Cremonese, G. (2010). The Mercury sodium atmospheric spectral imager for the MMO spacecraft of Bepi-Colombo. Planetary and Space Science, 58(1–2), 224–237. doi:10.1016/j.pss.2008.07.008